Fission fragment mass and energy distributions as a function of incident neutron energy measured in a lead slowing-down spectrometer

C. Romano,[1] Y. Danon,[1,*] R. Block,[1] J. Thompson,[1] E. Blain,[1] and E. Bond[2]

[1]*Rensselaer Polytechnic Institute, Department of Mechanical, Aerospace, and Nuclear Engineering, NES 1-25, 110 8th Street, Troy, New York 12180, USA*

[2]*Los Alamos National Lab, Los Alamos, New Mexico 87545, USA*

(Received 11 June 2009; revised manuscript received 5 November 2009; published 19 January 2010)

A new method of measuring fission fragment mass and energy distributions as a function of incident neutron energy in the range from below 0.1 eV to 1 keV has been developed. The method involves placing a double-sided Frisch-gridded fission chamber in Rensselaer Polytechnic Institute's lead slowing-down spectrometer (LSDS). The high neutron flux of the LSDS allows for the measurement of the energy-dependent, neutron-induced fission cross sections simultaneously with the mass and kinetic energy of the fission fragments of various small samples. The samples may be isotopes that are not available in large quantities (submicrograms) or with small fission cross sections (microbarns). The fission chamber consists of two anodes shielded by Frisch grids on either side of a single cathode. The sample is located in the center of the cathode and is made by depositing small amounts of actinides on very thin films. The chamber was successfully tested and calibrated using 0.41 ± 0.04 ng of ^{252}Cf and the resulting mass distributions were compared to those of previous work. As a proof of concept, the chamber was placed in the LSDS to measure the neutron-induced fission cross section and fragment mass and energy distributions of 25.3 ± 0.5 μg of ^{235}U. Changes in the mass distributions as a function of incident neutron energy are evident and are examined using the multimodal fission mode model.

DOI: 10.1103/PhysRevC.81.014607 PACS number(s): 25.85.Ec, 29.25.Dz, 29.30.Aj, 29.30.Ep

I. INTRODUCTION

There is currently a renewed interest in the measurement of fission fragment mass distributions of many of the actinides. Specifically, the changes in the mass yields as a function of incident neutron energy are important. Not only do these data enable a better understanding of the fission process, they are also critical for new reactor applications. In particular, fission yields as a function of incident neutron energy are necessary for accurate, detailed neutronics calculations for new reactors and fuels, as well as for stockpile stewardship applications. Yields of rare actinides are now important for calculations in fuel recycling and waste transmutation processes.

There is presently little information of the fission product mass distributions from neutron-induced fission for the majority of the actinides. Fission fragment mass yield data is only available for thermal, 0.5 MeV and 14 MeV incident neutron energies, and little or no data is available in the resonance regions. Chemistry measurements to determine the changes in symmetric fission of ^{235}U in the resonance regions were completed by Cowan *et al.* [1] in 1970. In 1989, Hambsch *et al.* [2] measured fragment yields and total kinetic energies (TKEs) of ^{235}U with a double-sided Frisch-gridded fission chamber in 50 individual resonances or resonance clusters up to 130 eV. The purpose of this experiment is to examine the changes in the fission fragment mass distributions of ^{235}U as a function of incident neutron energy from thermal energy to greater than 1 keV in the lead slowing-down spectrometer (LSDS). The current experiment verifies previous data by Hambsch *et al.* [2] and extends the data to 1400 eV. In the future, measurements of the less abundant actinides can be obtained in the LSDS because of its high neutron flux.

The double-sided Frisch-gridded fission chamber was developed [3–5] and used successfully in the past to measure mass and energy of fission fragments [6,7]. However, the high flux of the LSDS at Rensselaer Polytechnic Institute (RPI) provides the additional benefit of the ability to measure small samples (submicrograms) or those with small cross sections (microbarns). An additional benefit is the ability to measure the neutron energy-dependent fission cross section simultaneously with the fission fragment energies in the incident-neutron-energy range from below 0.1 eV to 1400 eV. This enables the detailed comparison of mass distribution changes as a function of incident neutron energy in the resonance regions. The useful cross-section energy range is limited by the LSDS resolution to 0.1 eV to 100 keV.

The fission chamber was first tested and calibrated with ^{252}Cf. This verified the function of the chamber and the development of the data analysis procedure. The tests with the ^{235}U sample in the LSDS verified that the concept of simultaneous measurement of incident-neutron-energy-dependent fragment mass distributions and cross section is feasible. It also verified that changes in the fragment mass distributions can be seen as a function of incident neutron energy.

II. THE LEAD SLOWING-DOWN SPECTROMETER

RPI's LSDS is a 75-ton, 1.8-m cube of lead. The lead is covered with a 0.75-mm layer of cadmium to prevent neutrons that have escaped and thermalized from re-entering the lead. The RPI 60-MeV electron linac creates neutrons through a (γ,n) reaction when the electrons interact with a tantalum target in the center of the lead. The neutrons slow down by

*Corresponding author: danony@rpi.edu

successive scattering collisions in the lead, creating a large isotropic flux attributable to the fact that a neutron can pass through the same region several times. The resulting neutron flux is about four orders of magnitude larger than an equivalent flight-path (5.6 m) time-of-flight experiment.

The neutron energy as a function of slowing-down time t in the LSDS [8] is determined by the equation

$$E(t) = \frac{k}{(t+0.3)^2}, \tag{1}$$

where $k = 165\,000\,\text{eV}\,\mu\text{s}^2$, t is in units of μs, and E is in units of eV. The k value was found using MCNP calculations and verified with actual measurements [9]. The energy-dependent neutron flux is proportional to the beam intensity and is given as [8]

$$\varphi(E) \propto E^{-0.776} e^{-(0.214/E)^{1/2}}. \tag{2}$$

These equations are then used to determine the energy-dependent, neutron-induced fission cross section as a function of neutron slowing-down time. The neutron-energy resolution [full width at half maximum (FWHM)] in the energy range of 0.1 eV to 1 keV is approximately 35% [8] and is in the range where the cross-section measurements and fragment mass distributions are most accurate. The fragment energy resolution is poor above 1 keV because of the noise induced in the system immediately after the linac pulse and will be explained in the next section.

III. FISSION CHAMBER AND ELECTRONICS

The fission chamber shown in Fig. 1 consists of two anodes shielded by Frisch grids on either side of a single cathode and is filled with CH_4 at 1 atm. The sample is deposited on a thin polyimide film located in the center of the cathode so that the fragments are emitted into each side of the chamber. The chamber, anode, and cathode are constructed of 6061 aluminum, and the grids are constructed of 0.08-mm-diameter copper-nickel wire wound around stainless-steel frames. The rods are ceramic with Teflon spacers. The distance from the cathode to the grid is 27 mm, which ensures that the fission fragments deposit their total energy in the gas, and the grid-to-anode distance is 6 mm. The grid design is based on design criteria discussed by Bunemann *et al.* [10]. The sample frame is constructed of two aluminum pieces with a 2500-Å polyimide film stretched over a 1.5-cm opening. This frame is constructed to fit into the center of the cathode so that the film is equidistant from the grids.

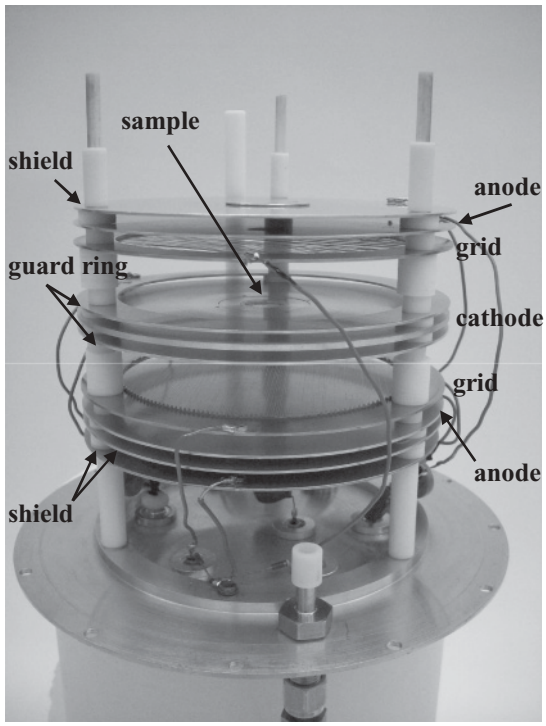

FIG. 1. Frisch-gridded fission chamber.

The LSDS is a difficult working environment because of the large amount of Bremsstrahlung radiation (γ flash) created when the electrons impact the tantalum target, as well as the high neutron flux. Gas-filled detectors are more resilient in the environment; however, the larger the volume of gas, the longer the recovery time of the system. The volume of gas is highly ionized by the γ flash, which causes the preamps to become saturated and then oscillate. Therefore, the critical design criteria for the fission chamber is to make the response time as fast as possible while maintaining the fission fragment energy resolution. This requires that the chamber be made as small as possible and filled with a gas with a high electron drift velocity; in this case CH_4 was selected. Also, the signals from the chamber must be processed as quickly as possible. The signals from the chamber are amplified with Cremat 110 [11] preamplifiers that have been modified to a shaping constant of 500 ns, which is slightly longer than the maximum time needed to collect the entire energy deposited in the gas (about 400 ns). The signal then travels through a 0.47-nf capacitor and is amplified by the shaping amplifier with a 0.2-μs time constant. A fast, pulsed switch is also placed between the chamber and the preamp to ground the signal during the γ flash. This is not a perfect solution because the switch also creates a large pulse when turning on, but it does improve recovery time by about 20 μs. The system's γ flash recovery time is approximately 12 μs for energy measurements and 5 μs for cross-section measurements.

The electronics diagram in Fig. 2, shows the system used when working in the LSDS. The cathode signal provides a gate to the analog-to-digital converter (ADC) as well as a trigger to the event scaler which records events as a function of the neutron slowing-down time. The linac pretrigger sends a signal prior to each linac pulse to the scaler to reset the time count and clear the memory and to the ADC to clear the memory. The linac pretrigger is also used to gate the signal switches to prevent the γ flash from saturating the preamps. The fragment energies and neutron slowing-down time are recorded for each linac pulse by RPI's data-acquisition software developed at Michigan State University [12]. The files are then prepared for offline analysis.

IV. ^{252}Cf MEASUREMENTS AND DATA ANALYSIS

Testing and calibration of the chamber and data-acquisition system was accomplished with a 0.41 ± 0.04-ng ^{252}Cf sample.

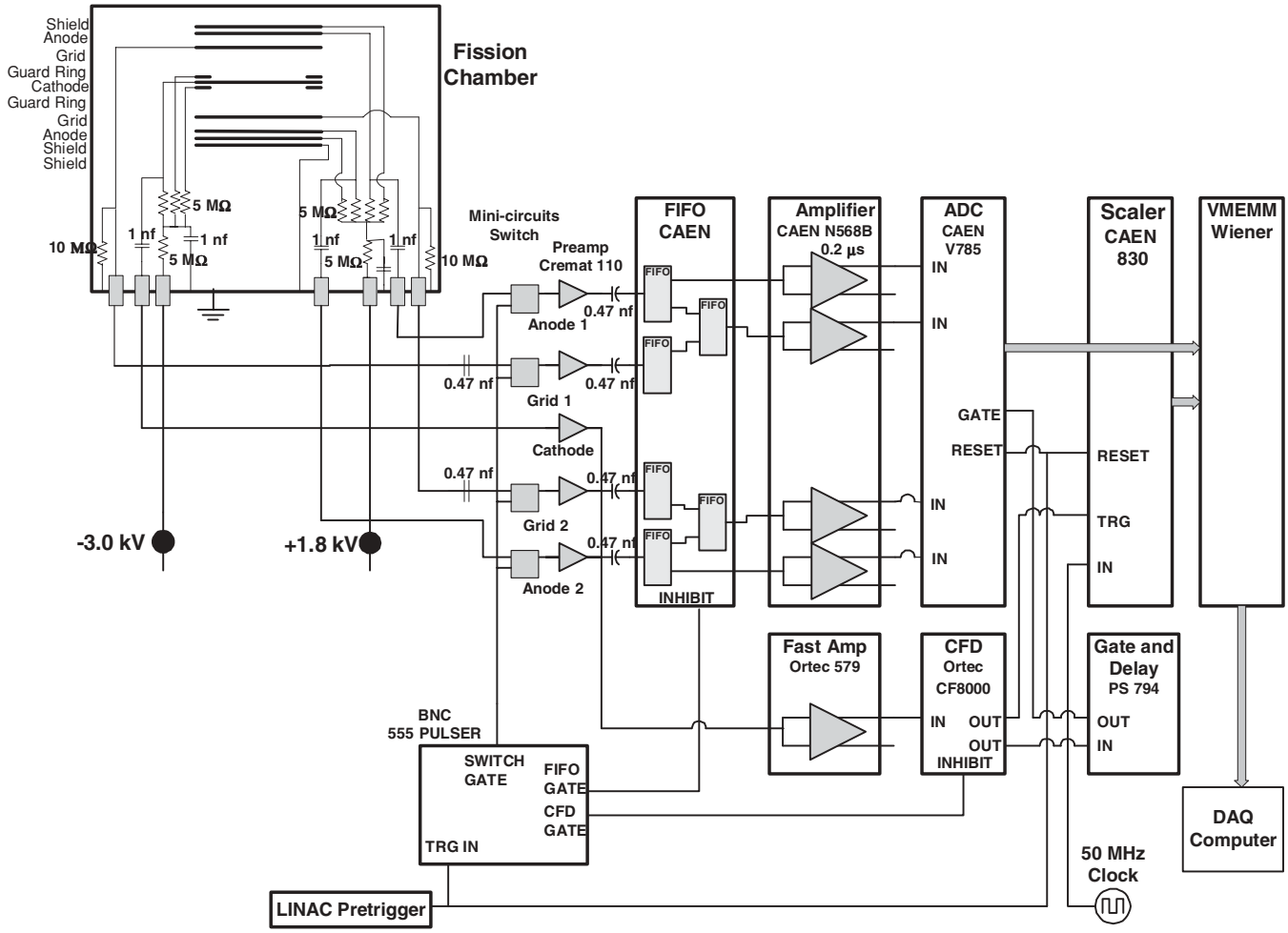

FIG. 2. Electronics and data-acquisition system for working in the LSDS.

The sample was made by dissolving ^{252}Cf in 0.1M HCl and depositing a known quantity on a polyimide film. This stippling method is not ideal because the sample can be lumpy, as is the case for this sample. The error attributable to the deposit method is minimized because the sample is so small; however, the energy resolution can become significantly poor for thicker samples.

The methods used for chamber calibration and energy corrections for the energy lost in the sample and the pulse height defect (PHD) have been described in great detail in Refs. [3–7], so it will not be discussed here. The iterative procedure to find the preneutron emission masses from the postneutron emission energies is that explained by Hambsch *et al.* [2]. The resulting postneutron emission mass and preneutron emission energy and mass distributions for ^{252}Cf is shown are Fig. 3. The postneutron emission mass is compared to the Evaluated Nuclear Data File (ENDF/B-VII.0) in the top plot. By nature of the double energy experiments, some of the fine structure is washed out. The ENDF values combine several types of experimental measurements, as well as theoretical models and, therefore, include more structure. In the bottom plot, the preneutron emission mass is compared to previous data by Hambsch *et al.* [7]. The excellent correlation of the mass distributions with previous work indicates that the chamber and electronics are working properly and the data analysis is correct. The resolution is slightly poorer than the Hambsch data and can be seen by the shallower dip in the symmetric fission. This is attributable to the sample deposit method, which causes large uncertainty in the energy lost in the sample, as well as error in the measured value of $\cos(\theta)$. Minor differences in the preneutron emission mass can be attributed to the variances in the average neutron emission data used.

V. ^{235}U CROSS SECTION AND MASS MEASUREMENTS

The ^{235}U sample was made at Los Alamos National Labs and was prepared by dissolving 99.98% ^{235}U in 8M HNO_3. The solution was dried down and redissolved in absolute alcohol and 25.3 ± 0.5 μg was deposited in an area of 1 cm diameter on a polyimide film. The chamber was placed in the LSDS for measurements. The linac was run at an average electron current of 8 μA, delivering 58-MeV electrons in a pulse width of 200 ns at 180 Hz. Simultaneous cross-section and energy measurements were obtained in a single 4-h run by tagging each event with the neutron slowing-down time. Figure 4 shows a scatter plot of the bare sample side-fragment energy

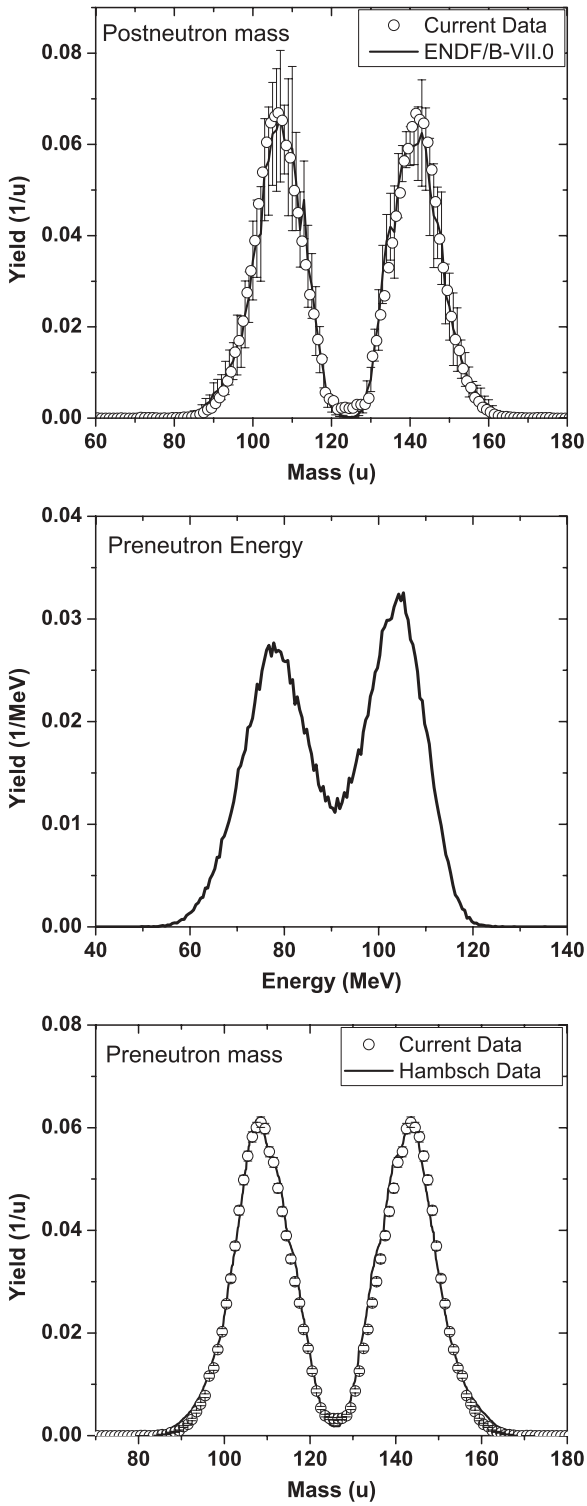

FIG. 3. (Top) ^{252}Cf spontaneous fission postneutron emission mass compared to ENDF/B-VII.0 (error bars are for ENDF data), (middle) current experiment preneutron emission energy distribution, and (bottom) preneutron emission mass compared to Hambsch [7] data (error bars are for statistical error on current data).

verses neutron slowing-down time. The two bands are the energy of the light and heavy fragment and the decrease in the number of events as a function of the neutron slowing-down time can be seen. When collecting data in the LSDS, the large γ flash saturates the preamps and creates a ringing in the signal as the preamps recover. This ringing was successfully removed from the data by utilizing a fast Fourier transform method.

Neutron fission cross-section measurements were previously obtained in the LSDS for ^{235}U, ^{238}U, ^{242,244,246,247}Cm, ^{254}Es, and ^{250}Cf [13–15]. The relative fission cross-section data for ^{235}U in the gridded chamber are shown in Fig. 5 compared to a previous cross-section measurement in the LSDS at RPI [15] and resolution-broadened ENDF/B-VII.0. The previous RPI cross-section measurement was based on a neutron time-energy correlation with a k value of 165 000 as given in Eq. (1). The k value for this experiment was found to be 175 000. This value was verified with MCNP5 calculations and is attributable to the large gas-filled space in and around the chamber. The broadened ENDF data were calculated using an MCNP simulation of the experimental conditions. The experimental results are in good agreement with the previous data and ENDF within the resolution of the LSDS, which indicates that cross-section measurements are easily measured simultaneously with fragment energies.

The cross section is calculated by first finding the incident neutron energy and flux as a function of time from Eqs. (1) and (2). The data are rebinned to create bins of width $\Delta E_i = f(dE/E)_i E_i$ (where f is a constant and $f < 1$) using the resolution function

$$\left[\frac{dE}{E}\right]_{\mathrm{FWHM}} = \left[0.0835 + \left(\frac{0.128}{E}\right) + 3.05 \times 10^{-5} E\right]^{1/2}. \tag{3}$$

The cross section is calculated using the equation

$$\sigma(E_i) = \frac{C_i}{F\phi(E_i)\Delta E_i}, \tag{4}$$

where E_i is the average energy in bin i, $\sigma(E_i)$ is the cross section at energy E_i, C_i is the number of counts in bin i, F is a normalization factor, and $\Delta E_i = E_i - E_{i-1}$ is the energy width of channel i [14,15].

The events used for the thermal mass distribution are those that occur when the mean neutron energy is at or below 0.1 eV. The neutron-energy resolution at 0.1 eV is 35%, but increases greatly below 0.1 eV because of energy upscattering. The resulting mass and energy spectra are plotted in Fig. 6. The postneutron emission mass distribution is compared to ENDF/B-VII.0 and the preneutron emission mass distribution is compared to previous data by Hambsch *et al.* [7]. The average neutron emission as a function of fragment mass and TKE was taken from a matrix of values by Maslin *et al.* [16]. The decrease in the width in the symmetric fission valley in our data compared to ENDF and Hambsch is attributable to the poorer resolution caused by the lumpiness of the sample.

VI. MASS DISTRIBUTIONS IN THE RESONANCES

To determine changes in mass distributions for ^{235}U as a function of incident neutron energy, data were extracted at and around each major resonance cluster peak that was discernible in the neutron slowing-down time data between 0.1 eV and 1 keV, as shown in Fig 7.

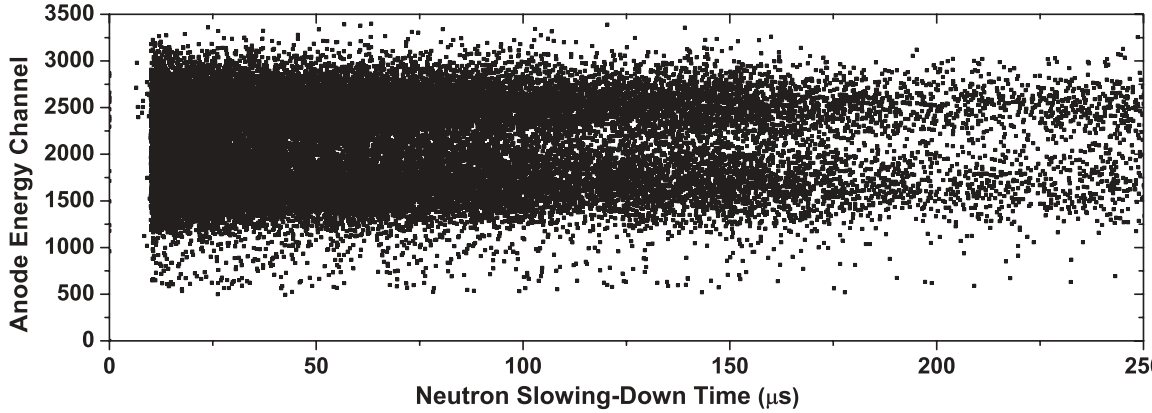

FIG. 4. Anode energy distribution as a function of neutron slowing-down time in the LSDS.

A. Multimodal fission model

The variations of mass distributions in the resonance regions are the result of variations in the probability of fission in each of the three fission exit channels for ^{235}U fission. These fission channels were first formalized by Straede *et al.* [17] and Brosa *et al.* [18] and are composed of the Standard I, Standard II, and Superlong modes and can be described by a set of five Gaussians for ^{235}U fitted to the fission mass spectrum by the equation

$$Y(M) = \sum_{1}^{2} \frac{W_m}{\sqrt{2\pi}\sigma_m} \left\{ e^{-(M-M_m)^2/2\sigma_m^2} + e^{-[M-(236-M_m)]^2/2\sigma_m^2} \right\} + \frac{W_m}{\sqrt{2\pi}\sigma_m} \{ e^{-(M-118)^2/2\sigma_m^2} \}, \quad (5)$$

where W_m and σ_m are the Gaussian strength and width, respectively, and M_m is the average mass. The first term describes the Standard I and Standard II modes and the second term describes the symmetric Superlong mode. Of the three channels, Standard II is the primary channel for thermal fission and is centered on a fragment mass near 141 and 95 [2]. It is characterized by a moderate TKE. Standard I mode is slightly more symmetric than Standard II and is characterized by a mass split around 134 and 102 and a high TKE attributable to the increased Coulomb repulsion of the shorter scission shape. The Superlong mode is symmetric and has the lowest TKE of the three modes because of the elongated shape at scission [19].

A least-squares fit of the five Gaussians described in Eq. (5) for the thermal distribution for ^{235}U is shown in Fig. 8. The fit is very sensitive to the guess values and several differing fits with good χ^2 values can be found. The width of the Superlong mode is particularly difficult because the solutions can be divergent or vary inconsistently [2,17,20,21]. The Superlong mode average mass is fixed at $M_{SL} = 118$, and the width σ_{SL} may also have to be fixed to a theoretical value; in this case $\sigma_{SL} = 4.88$, based on work by Brosa *et al.* [20]. When comparing changes in fission modes, consistency in the fit is important. Therefore, once the thermal fit is found, the widths σ_m and average masses M_m of each mode are fixed and only the strength of each Gaussian is allowed to vary. With this method, changes in the heavy mass distribution can readily be examined by comparing the weight of the Gaussians describing fission in each of the Standard I and Standard II fission channels. It is easier to compare the symmetric fission by using a valley-to-peak ratio attributable to the small amount of symmetric fission data and the inconsistency of the symmetric fit.

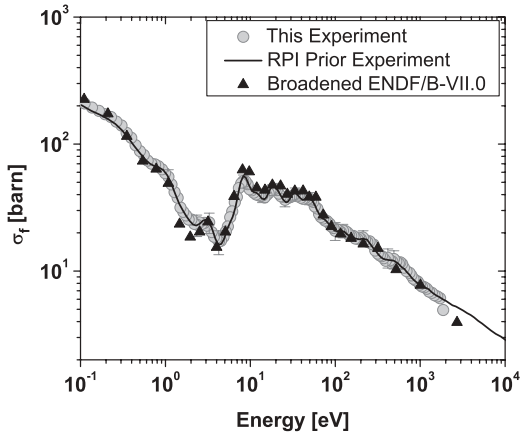

FIG. 5. ^{235}U fission cross section compared to previous cross-section measurement in the LSDS at RPI. [15].

B. Symmetric fission

Table I and Fig. 9 compare symmetric fission as a function of incident neutron energy (or excitation energy). The data show specific trends and are in agreement, except for resonance region 5, with previous data by Hambsch *et al.* [2] and radiochemistry measurements by Nasuhoglu *et al.* [22] and Faler and Tromp [23]. The radiochemistry measurements involve the ratio of the quantities of either ^{98}Sr or ^{99}Mo compared to ^{115}Cd resulting from fission at various incident neutron energies. The ratio at specified incident neutron energies is compared to the ratios at thermal energies to determine the R value. The R value, as defined in Ref. [23], is written as

$$R = \frac{A'_{asy}/A'_{sym}}{A_{asy}/A_{sym}}, \quad (6)$$

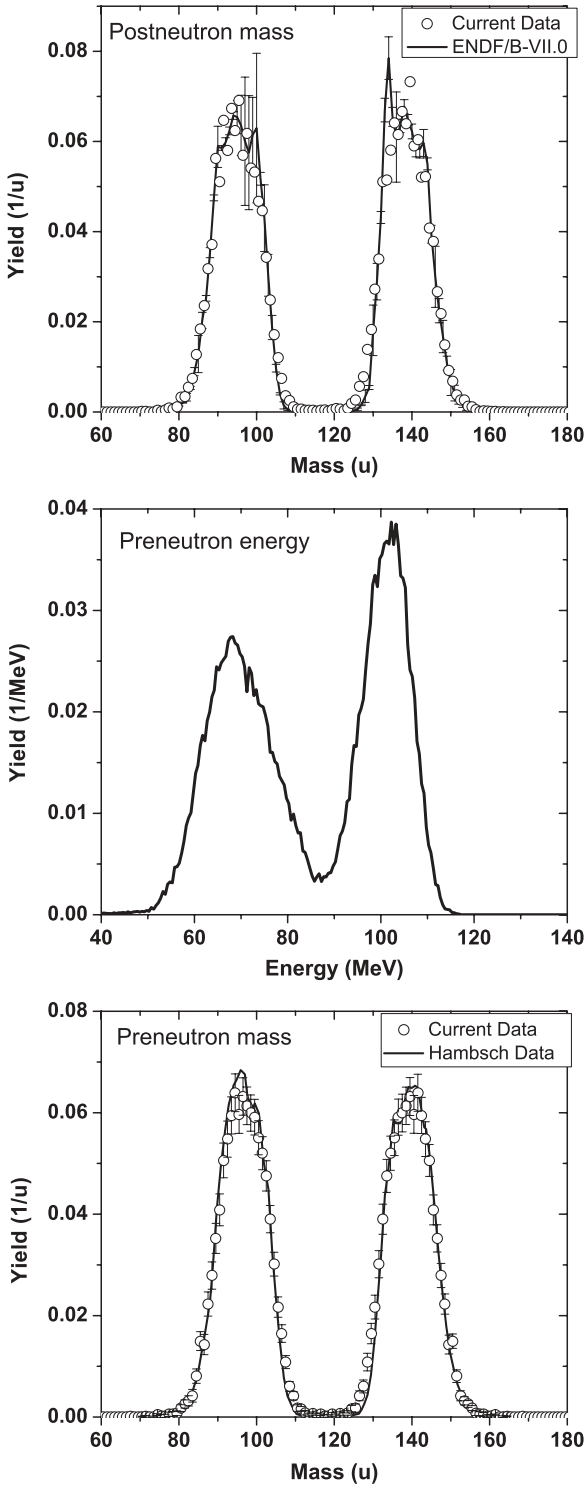

FIG. 6. (Top) ^{235}U thermal postneutron emission masses compared to ENDF/B-VII.0 (error bars are for ENDF data), (middle) thermal preneutron emission energy spectrum, and (bottom) thermal preneutron emission masses compared to Hambsch [7] (error bars are for statistical error on current data).

where A'_{asy} is the quantity of ^{98}Sr or ^{99}Mo, A'_{sym} is the quantity of ^{115}Cd at a specific neutron energy, and A_{asy} and A_{sym} are the values at thermal. Therefore, $R = 1$ at thermal. For double

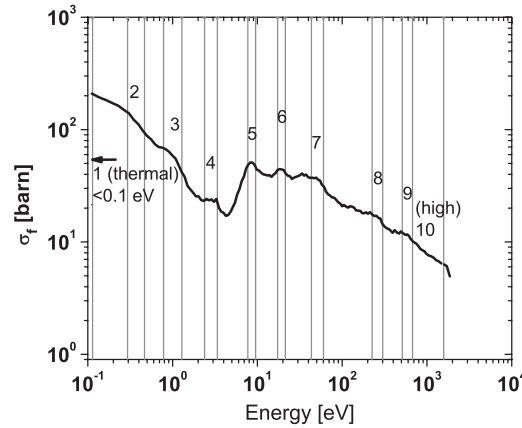

FIG. 7. Boundaries of the numbered resonance region data used to examine mass distributions as a function of the neutron-energy channel.

energy measurements, a $(V/P)_{\text{ratio}}$ is commonly used and is given by [2]

$$\left(V/P\right)_{\text{ratio}} = \frac{\left(V/P\right)_{\text{resonance}}}{\left(V/P\right)_{\text{thermal}}}. \tag{7}$$

The value of V is the sum of the fission yield of masses 115 to 121, which comprise the valley in the mass distribution. The value of P is generally taken as a sum in the peak region, but an accurate picture of what is happening in the valley cannot be seen if the peak values vary as well. Therefore, the value of P is taken as the average yield of the entire mass distribution, which is a constant value of 2 for all incident neutron energies. The values of P cancel and the ratio becomes

$$V_{\text{ratio}} = V_{\text{resonance}}/V_{\text{thermal}}. \tag{8}$$

In Table I and Fig. 9, the V_{ratio} is compared is compared to previous $(V/P)_{\text{ratio}}$ data as well as 1 R values for the chemistry measurements.

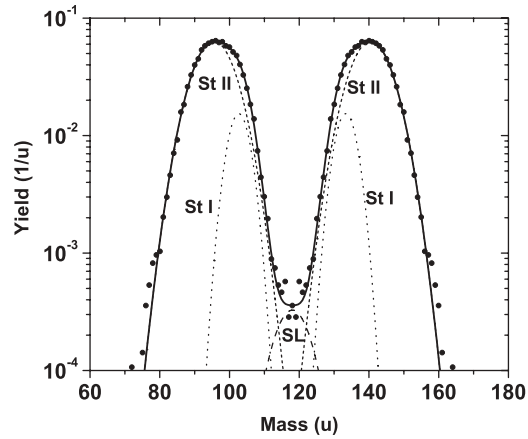

FIG. 8. Five Gaussian fits describing the three fission modes for ^{235}U. The points are the data and the solid line is the sum of the three modes.

TABLE I. Valley ratios V_{ratio} in resonance regions compared to thermal energies. Where applicable, resonances measured by Hambsch *et al.* [2] are shown. When the current data include several values of Hambsch's data, the average value of V/P is used for comparison. The $1/R$ values are chemistry measurements.

Region No.	Energy range (eV)	V_{ratio}	Included Hambsch resonances (eV)	V/P Hambsch *et al.* [2] data (%)	$1/R$ Faler[a] and Nasuhoglu[b]	TKE (MeV)
1	<0.1	1	<0.1	1	1	170.93 ± 0.08
2	0.29–0.46	1.12 ± 0.34	0.3	–	1.35[a]	171.09 ± 0.08
3	0.78–1.29	1.13 ± 0.35	1.14	1.28 ± 18	1.18 ± 0.20[b]	171.14 ± 0.08
4	2.38–3.37	0.47 ± 0.21	3.1	0.34 ± 35	0.73 ± 0.20[b]	171.13 ± 0.08
5	7.71–9.53	1.36 ± 0.42	8.77	0.72 ± 10		171.00 ± 0.08
			9.28	0.84 ± 20		
			Average	0.78		
6	17.34–21.37	0.78 ± 0.26	19.30	0.57 ± 12		171.11 ± 0.08
			20.17	1.36 ± 27		
			Average	0.965		
7	43.4–60.24	0.87 ± 0.26	46.8–47.0	0.85 ± 25		171.25 ± 0.08
			47.4–49.7	1.17 ± 16		
			49.9–52.7	0.81 ± 15		
			54.5–56.9	0.63 ± 16		
			57.2–59.1	1.01 ± 19		
			Average	0.894		
8	225–275	0.54 ± 0.21		–		171.0 ± 0.08
9	511–675	1.40 ± 0.44		–		170.89 ± 0.08
10	675–1400	1.13 ± 0.30		–		171.55 ± 0.08

[a] $1/R$ value based on chemical ratios of ^{115}Cd and ^{99}Mo [23].
[b] $1/R$ value based on chemical ratios of ^{115}Cd and ^{89} Sr [22].

The Nasuhoglu article indicates that the symmetric fission was greater than thermal at a neutron energy of 1.1 eV ($1/R = 1.18$), but significantly lower than thermal at 3.1 eV ($1/R = 0.73$) and slightly lower than thermal at 9.5 eV ($1/R = 0.91$). Faler and Tromp [23] indicated that the 0.28-eV resonance shows an increase in symmetric fission ($1/R = 1.35$). Our data agree with these experiments in that the 0.28- and 1.1-eV resonance shows increased symmetric fission, and the 3.1-eV region shows the greatest decrease in symmetric fission.

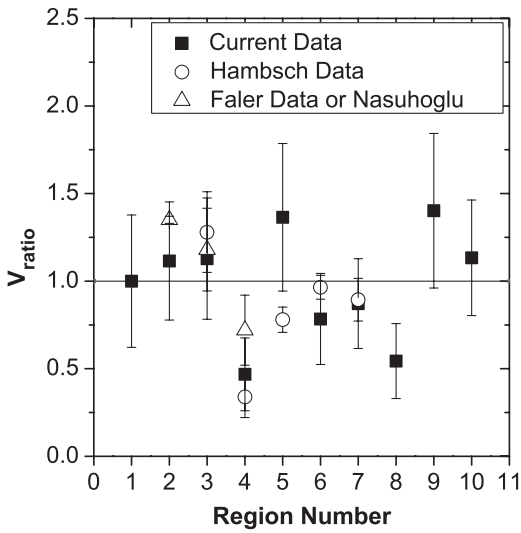

FIG. 9. Plot of valley ratios in the resonance regions listed in Table I [2,22,23].

The Hambsch data indicate a decrease in symmetric fission in regions 4–7. The current data agree with Hambsch's data, except at 8.77 eV (resonance region 5). The disagreement in region 5 may be attributable to quickly changing fission responses evidenced by the rapidly changing cross section at energies just below 8.77 eV. The result in region 5 may also be influenced by the increase in symmetric fission as measured in the 5.2–6.1 and 6.38 resonances by Hambsch *et al.* where the values of V_{ratio} are 1.63 and 1.29, respectively. This would influence the current data because of the broad LSDS neutron-energy resolution ($\Delta E/E$ is about 35%). The current data extend to greater than 1 keV and two additional resonance regions are examined. At about 250 eV in resonance region 8 there is decreased symmetric fission, as well a large decrease in TKE. This region will be discussed in greater depth later. There is a significant increase in symmetric fission, resulting in a V_{ratio} of 1.4 around the 500-eV energy region. The higher excitation energy may cause the nucleus to prefer the symmetric fission barrier, unlike the lower energy regions.

C. Standard I and Standard II fission modes

The heavy mass peak can be fitted to two Gaussians, which represent Standard I and Standard II of the three fission modes. First, the thermal region heavy mass data were fit to two Gaussians and the widths, center locations, and weights were determined. For the rest of the resonance regions, the width and center location were fixed to the thermal value and only the weights ($W1$ and $W2$) were allowed to vary. The ratio of the weight of Standard I to Standard II was determined for

TABLE II. Standard I and Standard II weight ratios $(W1/W2)_{\text{ratio}}$ in resonance regions compared to thermal energies. Where applicable, resonances measured by Hambsch *et al.* [2] are shown. When the current data include several values of Hambsch's data, the average value of $(W1/W2)_{\text{ratio}}$ is used for comparison.

Region No.	Energy range (eV)	$(W1/W2)_{\text{ratio}}$	Included Hambsch resonances (eV)	Hambsch *et al.* [2] $(W1/W2)_{\text{ratio}}$
1	<0.1	1	<0.1	1
2	0.29–0.46	0.994 ± 0.04		–
3	0.78–1.29	1.021 ± 0.043	1.14	1.025 ± 0.027
4	2.38–3.37	1.101 ± 0.064	3.14	1.160 ± 0.029
5	7.71–9.53	1.001 ± 0.047	8.77	1.058 ± 0.025
			9.28	1.081 ± 0.030
			Average	1.070
6	17.34–21.37	1.092 ± 0.047	19.30	1.206 ± 0.027
			20.17	1.120 ± 0.038
			Average	1.163
7	43.4–60.24	1.082 ± 0.034	46.8–47.0	1.093 ± 0.030
			47.4–49.7	1.074 ± 0.028
			49.9–52.7	1.052 ± 0.026
			54.5–56.9	1.155 ± 0.025
			57.2–59.1	1.157 ± 0.031
			Average	1.106
8	225–275	1.009 ± 0.054		–
9	511–675	1.004 ± 0.051		–
10	675–1400	1.024 ± 0.036		–

each resonance using the equation

$$\left(W1/W2\right)_{\text{ratio}} = \frac{\left(W1/W2\right)_{\text{resonance}}}{\left(W1/W2\right)_{\text{thermal}}}. \tag{9}$$

Changes in the weight ratios in the resonance regions were compared to Hambsch's data and are shown in Table II and Fig. 10.

D. Changes in total kinetic energy

Changes in the TKE of the fission fragments in the resonance regions is also examined in the form of

$$\text{TKE}_{\text{dif}} = \text{TKE}_{\text{resonance}} - \text{TKE}_{\text{thermal}}, \tag{10}$$

where $\text{TKE}_{\text{thermal}} = 170.93$ MeV. The values of TKE_{dif} are plotted in Fig. 11. The TKE tends upward with increased excitation energy; however, the increase of TKE is greater than the increase in incident neutron energy. This can be explained by a change in the proportion of fissions in each of the three fission modes for ^{235}U.

The larger the value of the weight ratio, the greater the increase in the Standard I fission mode and the greater the value of the average TKE due to the short scission shape of the Standard I fission mode. This correlation of the TKE and

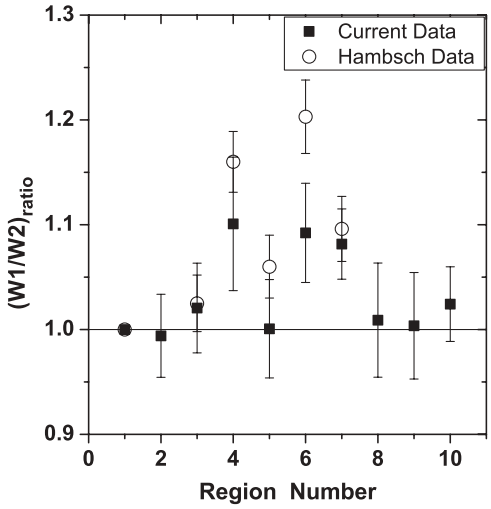

FIG. 10. Change in Standard I and Standard II fission modes as a function of incident neutron energy.

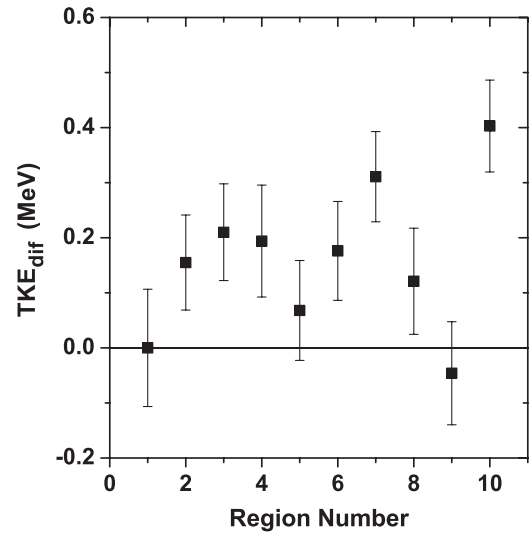

FIG. 11. Change in TKE as a function of incident neutron energy.

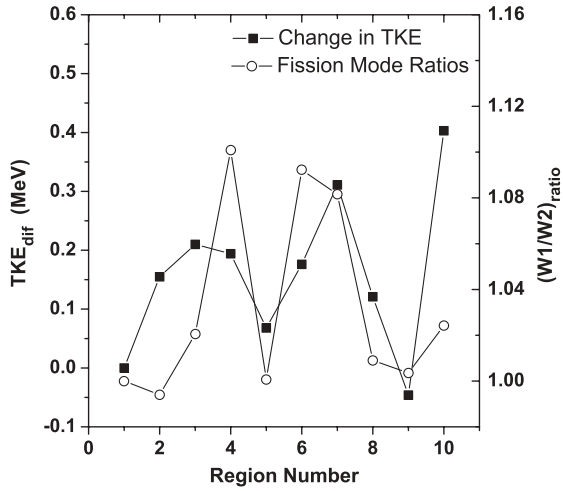

FIG. 12. Comparison of TKE trends and fission mode ratio trends in each resonance region.

the fission mode ratios is easily seen in Fig. 12 and is as expected. Variations in the correlation come into play when the low TKE Superlong mode becomes more prominent. It is interesting to note that the resonance regions with the least amount of symmetric fission (Superlong mode) have higher weights of the Standard I fission mode. The best example of this is resonance region 4, where symmetric fission was the lowest and Standard I was the strongest of all the resonance regions. Another example is resonance region 9, where symmetric fission was the largest of the regions and the Standard I strength was relatively low. This resulted in a relatively low average TKE when taking into account the incident neutron energy of a little over 0.5 keV.

There is also an anticorrelation between the V_{ratio} and the $(W1/W2)_{\text{ratio}}$, indicating that Standard I fission decreases as the Superlong mode increases. This is shown in Fig. 13. The anticorrelation breaks down in resonance region 8, where both the Superlong and Standard I modes show a reduced amount of fission than thermal, which indicates that the Standard II mode dominates.

E. Resonance region 8

Resonance region 8, shown in Fig. 14, has an interesting structure, with a higher preneutron emission yield of the 96/140 split when compared to thermal or other resonance regions. Although the sample thickness causes a decrease in the precision of the measurement, studying the mass distribution in the resonances relative to the thermal distribution can readily show significant changes with incident neutron energy. The incident-neutron-energy range for the data in this resonance group is primarily 225–275 eV. The increase in the Standard II fission mode is accompanied by a decrease in the symmetric Superlong mode when compared to thermal, as well as a ratio of Standard I to Standard II near thermal values. The reason for this behavior is unknown, but may be attributable to a strong transmission probability of the Class II states in the second well of the Standard II fission barrier [19], and the strong shell effects indicate a low excitation energy. It would

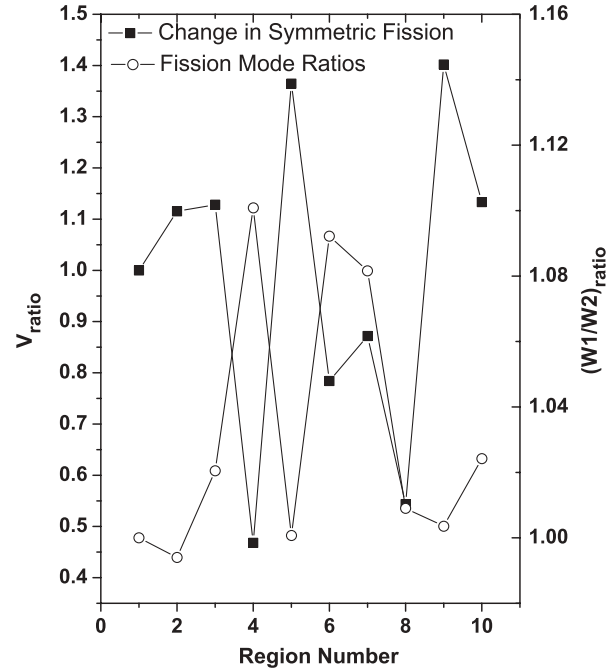

FIG. 13. The anticorrelation between the quantity of the Superlong mode symmetric and the Standard I mode fission.

be interesting to examine this resonance region further with a higher resolution neutron source to pinpoint the exact incident neutron energy where this behavior is prominent. Of course, this data must be verified with additional experiments to ensure that these effects are not a statistical anomaly.

F. Resonance region 9

Resonance region 9 includes the incident-neutron-energy range around 511–675 eV. The mass distribution in the top plot of Fig. 15 shows an increase in symmetric fission. Shell effects are still prevalent in this energy region and the increased

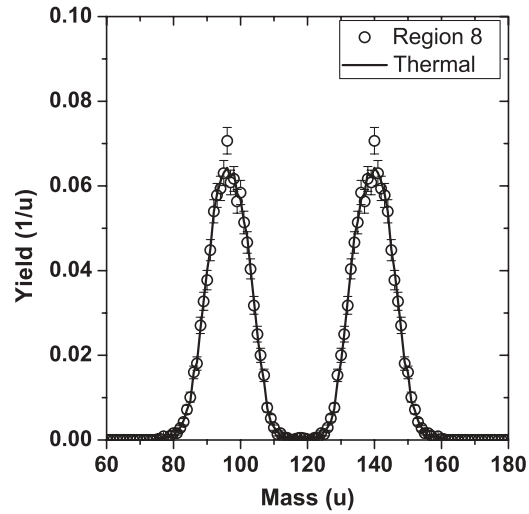

FIG. 14. Mass distribution of resonance region 8 compared to thermal.

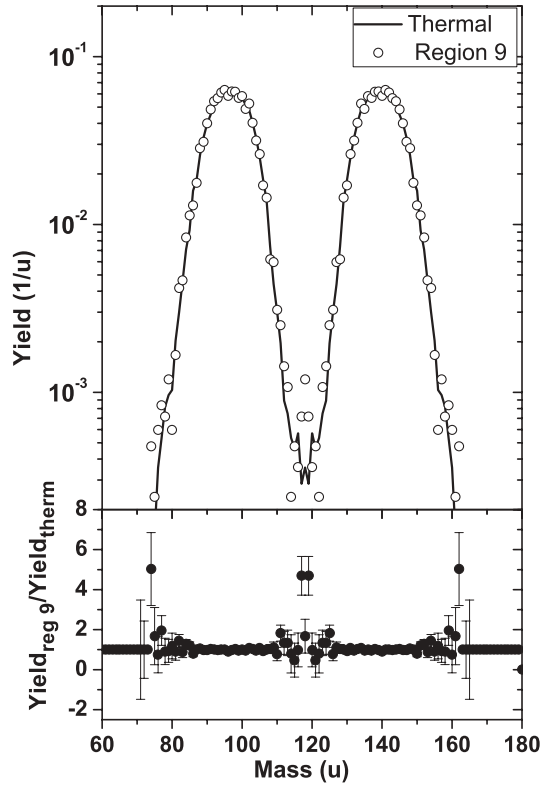

FIG. 15. (Top) Resonance region 9 mass distribution compared to thermal, (bottom) mass yield at resonance region 9 divided by yield at thermal.

preference for the Superlong channel is likely attributable to the structure of the compound nucleus in the second minimum of the double-humped barrier. The bottom plot of Fig. 15 shows the mass yield at resonance 9 divided by the mass yield at thermal. This plot not only emphasizes the increase in symmetric fission compared to thermal, but also indicates an increase in very asymmetric fission. The increase in very asymmetric fission may be attributed to the superlong fission mode, as indicated by computer modeling by Talou *et al.* [24], where the far ends of the Gaussian describing the Superlong mode extended into the very asymmetric region. It could also indicate an additional Superasymmetric mode at this excitation energy. The statistics in the Superasymmetric masses are poor and these data should be confirmed.

VII. CONCLUSION

This experiment verifies previous data of fission yields and TKE as a function of incident neutron energy for ^{235}U, and it extends the existing data from 100 to 1400 eV. Correlations were found among the V_{ratio}, $(W1/W2)_{\text{ratio}}$, and TKE_{dif}. TKE_{dif} and $(W1/W2)_{\text{ratio}}$ are correlated, indicating that, in general, the TKE increases as fission in the Standard I mode increases. These results are a verification of the data by Hambsch *et al.* [2]. An anticorrelation of the V_{ratio} with the $(W1/W2)_{\text{ratio}}$ was found meaning that as symmetric fission increased, fission in the Standard I mode decreased. This may indicate a competition between the Superlong channel and the Standard I channel.

The exception to the general trend was region 8 (225–275 eV), where symmetric fission was low (well below the thermal value), the weight of the Standard I fission was also low (near the thermal value) and the TKE was about 100 keV above thermal. The decrease in Standard I fission would generally result in a lower TKE. The reason for this phenomenon is uncertain and it would be interesting to investigate further.

This experiment also is verification that the double-gridded fission chamber can successfully be placed in the LSDS to simultaneously obtain fission fragment energy and cross-section measurements and that changes in mass distributions as a function of incident neutron energy can be seen. It is significant to note that all ^{235}U data were obtained in a single 4-h run with a 25.3-μg sample. Despite the lower mass resolution when compared to previous experiments because of the lumpy sample, the thermal mass distribution can easily be compared to mass distributions in the resonance regions to point out changes in fission characteristics. Of these characteristics, changes in symmetric fission, average heavy mass, and TKE were observed. Measurement in the LSDS has the ability to examine data as a smooth function of incident neutron energy from thermal to greater than 1 keV, which gives the ability to find regions of interest for further study that may not have been evident from previous experiments. Because of the high neutron flux, it is also the only method available for studying the change in mass distributions of very small (microgram) samples with incident neutron energies from thermal to greater than 1 keV.

Additional efforts can be made to improve fragment energy resolution through the use of vacuum-evaporated samples. Also, investigations in the thermal energy region can be improved by slowing the linac pulse rate to allow additional collection of data in the very low neutron-energy range. The incident neutron-energy resolution cannot be improved because it is intrinsic to the LSDS; however, it has proved to be acceptable for mass-distribution comparisons in resonance regions and some isolated lower-energy resonances.

ACKNOWLEDGMENTS

The authors express their appreciation to the Linac staff for their expertise and diligent work in running the Linac during the experiments. The authors also thank the Stewardship Science Academic Alliance for their funding of this research, Grant No. DE-FG03–03NA00079.

[1] G. A. Cowan, B. P. Bayhurst, R. I. Prestwood, J. S. Gilmore, and G. W. Knobeloch, Phys. Rev. C **2**, 615 (1970).
[2] F.-J. Hambsch, H.-H. Knitter, and C. Budtz-Jorgensen, Nucl. Phys. **A491**, 56 (1989).
[3] C. Budtz-Jorgensen and H.-H. Knitter, Nucl. Instrum. Methods **223**, 295 (1984).
[4] C. Butdtz-Jorgensen, H.-H. Knitter, and G. Bortels, Nucl. Instrum. Methods A **236**, 630 (1985).

[5] C. Butdtz-Jorgensen, H. Knitter, C. Streade, F. Hambsch, and R. Vogt, Nucl. Instrum. Methods A **258**, 209 (1987).
[6] F.-J. Hambsch, in *Proceedings of the International Workshop on High-Resolution Spectroscopy of Fission Fragments, Neutrons, and γ-Rays* (Dresden, Germany, 1993).
[7] F.-J. Hambsch, J. Van Aarle, and R. Vogt, Nucl. Instrum. Methods A **361**, 257 (1995).
[8] R. E. Slovacek, D. S. Cramer, E. B. Bean, R. W. Hockenbury, J. R. Valentine, and R. C. Block, Nucl. Sci. Eng. **62**, 455 (1977).
[9] R. C. Block, R. W. Hockenbury, R. E. Slovacek, E. B. Bean, and D. S. Cramer, Phys. Rev. Lett. **31**, 247 (1973).
[10] O. Bunemann, T. E. Cranshaw, and J. A. Harvey, Can. J. Res. A **27**, 191 (1949).
[11] Cremat, Inc., Watertown, MA.
[12] R. Fox, Michigan State University (private communication).
[13] C. Romano, Y. Danon, R. C. Haight, S. Wender, D. Vieira, E. Bond, R. Rundberg, J. Wilhelmy, J. O'Donnell, A. Michaudon, T. Bredeweg, D. Rochman, T. Granier, and T. Ethvignot, Nucl. Instrum. Methods A **562**(2), 771 (2006).
[14] Y. Danon, R. E. Slovacek, R. C. Block, R. W. Lougheed, R. W. Hoff, and M. S. Moore, Nucl. Sci. Eng. **109**, 341 (1991).
[15] Y. Danon, master's thesis, Rensselaer Polytechnic Institute, 1990.
[16] E. E. Maslin, A. L. Rodgers, and W. G. F. Core, Phys. Rev. **164**, 1520 (1967).
[17] Ch. Straede, C. Budtz-Jorgensen, and H.-H. Knitter, Nucl. Phys. **A462**, 85 (1987).
[18] U. Brosa, S. Grossmann, and A. Muller, Z. Naturforsch A **41**, 1341 (1986).
[19] C. Wagemans, *The Fission Process* (CRC Press, Boca Raton, FL, 1991).
[20] U. Brosa, H.-H. Knitter, T.-S. Fan, J.-M. Hu, and S.-L. Bao, Phys. Rev. C **59**, 767 (1999).
[21] S. Oberstedt, F.-J. Hambsch, and F. Vivés, Nucl. Phys. **A644**, 289 (1998).
[22] R. Nasuhoglu, S. Raboy, G. R. Ringo, L. E. Glendenin, and E. P. Steinberg, Phys. Rev. **108**, 1522 (1957).
[23] K. T. Faler and R. L. Tromp, Phys. Rev. **131**, 1746 (1963).
[24] P. Talou, in *Conference Proceedings of the International Conference on Nuclear Data for Science & Technology* (EDP Sciences, Les Ulis, France, 2007).